frontiers | Frontiers in Physics

TYPE Original Research
PUBLISHED 23 January 2026
DOI 10.3389/fphy.2025.1732657

OPEN ACCESS

EDITED BY
Yiying Feng,
Suzhou University, China

REVIEWED BY
Avtar Singh,
Adama Science and Technology University, Ethiopia
Suresh Balanethiram,
National Institute of Technology Puducherry, India

*CORRESPONDENCE
Ghada A. Khouqeer,
gkhouqeer@imamu.edu.sa

RECEIVED 26 October 2025
REVISED 22 December 2025
ACCEPTED 23 December 2025
PUBLISHED 23 January 2026

CITATION
Dastidar A, AbdelAll N, Patra TK, Mohapatra SK, Pradhan KP and Khouqeer GA (2026) Tapered dielectric quad-cavity MOSHEMT: a double-gate design for enhanced biosensing. *Front. Phys.* 13:1732657.
doi: 10.3389/fphy.2025.1732657

Tapered dielectric quad-cavity MOSHEMT: a double-gate design for enhanced biosensing

Ananya Dastidar[1], Naglaa AbdelAll[2], Tapas Kumar Patra[1], S. K. Mohapatra[3], K. P. Pradhan[4] and Ghada A. Khouqeer[2]*

[1]School of Electronic Sciences, Odisha University of Technology and Research, Bhubaneswar, India, [2]Physics Department, Faculty of Science, Imam Mohammad Ibn Saud Islamic University (IMSIU), Riyadh, Saudi Arabia, [3]School of Electronics Engineering, Kalinga Institute of Industrial Technology (KIIT) Deemed to be University, Bhubaneswar, Odisha, India, [4]Department of ECE, Indian Institute of Information Technology, Design and Manufacturing, Kancheepuram, Chennai, India

Rapid and accurate biomolecule detection is vital for next-generation diagnostic and sensing technologies. Reliable biosensing has driven innovations in transistor-based detection platforms. In this work, a quad-cavity double-gate tapered dielectric metal oxide-semiconductor high electron mobility transistor (MOSHEMT) is investigated using technology computer-assisted design (TCAD) simulations for biosensing applications. The proposed structure leverages dielectric modulation and taper cavity geometry to improve electrostatic control and charge sensitivity. Comparative analysis with conventional architectures, including single-gate single-cavity, single-gate dual-cavity, and double-gate non-tapered quad-cavity MOSHEMTs, demonstrates improvements of 54%, 25%, and 84% in drain current sensitivity, respectively. Parametric variation of the taper angle reveals that 60° provides optimal sensitivity due to the enlarged effective surface area for biomolecule binding. Moreover, the device maintains reliable detection capability for biomolecule fill factors as low as 15%, indicating its suitability for low-concentration biosensing environments.

KEYWORDS

biosensing, dielectric modulation, metal oxide-semiconductor high electron mobility transistor, tapered dielectric technology, computer-assisted design

1 Introduction

High-electron mobility transistor (HEMT) metal oxide-semiconductor high electron mobility transistor (MOSHEMT)-based sensors, utilizing wide bandgap semiconductors, have garnered considerable attention, as they offer a high sensitivity owing to their increased electron mobility, impressive frequency response, low noise levels, and minimal power consumption [1–5]. In biosensing applications, AlGaN/GaN MOSHEMT biosensors play a pivotal role in detecting alterations in surface charge resulting from biomolecular binding or chemical interactions due to the two-dimensional electron gas (2DEG) formed at the AlGaN/GaN interface [6–8]. MOSHEMT biosensors are characterized by their sensitivity, selectivity, and limits of detection, which are determined by variations in electrical parameters resulting from physical or chemical changes at the gate sensing area of the devices upon binding of biological molecules [9–12]. Several research groups have elucidated these sensing metrics using analytical techniques and physics-based models to comprehend the operational mechanism

of HEMT biosensors [13–16]. These crucial electrical parameters, including drain current, threshold voltage, channel potential, channel conductance, surface potential, capacitance, transconductance, and conductance-to-current ratio, among others, aid in understanding deviations in device characterization from a neutral response [17–19].

When compared to a single-gate MOSHEMT, double-gate structures have advantages in terms of performance, scalability, and reliability [20, 21]. Double-gate structures provide better control of the gate over the channel than single-gate structures. This improves electrostatic integrity and reduces leakage current, thereby resulting in higher ON/OFF current ratios as well as enhancing device performance [22]. They also offer effective modulation of the channel due to the presence of two gates; thus, it can exhibit improved subthreshold swing for lower power consumption and enhanced efficiency. They mitigate short-channel effects (SCE) such as drain-induced barrier lowering (DIBL) and subthreshold slope (SS) degradation [23, 24]. Two gates confine the electric field more effectively, limiting its impact to SCEs and allowing for better scalability on smaller devices. However, comparing them with single-gate counterparts shows that double-gated structures generally have lower values of this capacitance [25, 26]. With the inception of double-gate devices, the trend toward analyzing multi-gate devices with alternative materials for the gate, insulator, and substrate is increasing. A DG InP/InGaAs structure was presented in [27], where TCAD simulation was performed for gate and barrier dimension variations. The proposed device exhibited improved device parameters except for SS and Ion/Ioff. A double delta-doped DG-MOSHEMT with a multi-cap layer with a thin InAlAs barrier with HfO_2 as a dielectric material finds use in the high-frequency domain. Maximum transconductance and higher cut-off frequency were reported when compared with an SG-HEMT structure [28]. Simulation of an underlap double-gate (U-DG) AlGaN/GaN MOSHEMT with HfO_2 as the gate oxide improved analog performance over a Schottky HEMT, thereby making it suitable for high-power enhanced frequency devices [29]. A symmetric U-DG GaN/AlGaN MOS-HEMT with a doped AlGaN barrier and spacer of varying width showed that the reduction in the width of the doped region leads to improved gate control as well as high ON current when examined for its effect on the analog figure of merits (FoMs) [18]. The device performance of a DG n-AlGaN/GaN MOSHEMT, where the doping concentration of the AlGaN was moderated, compared with a conventional HEMT as well as a metal-oxide-semiconductor field-effect transistor (MOSFET) device [30]. A DG underlap AlInN/GaN MOSHEMT for analog and radio frequency (RF) performance measurements using a TCAD tool shows that, through gate length and underlap length scaling, there is an increase in the device parameter values like drain current, transconductance, and frequency, but it caused a drop in the on-resistance of the simulated device. Results indicate the device's potential for use in high-power, high-frequency applications [22]. An increase in effective barrier thickness exhibited an increase in drain current and SCE, like DIBL and SS. A reduction in delay and a negative shift in threshold voltage have also been observed. A decrease in barrier thickness was associated with an increase in gate capacitance, output resistance, transconductance, and improved cut-off and maximum oscillation frequency [31]. Currently, the trend is moving toward biomedical applicability of double-gate structures [32–34]. Biosensors have been implemented by using a cavity near the gate or by coating the gate with bio-analyte to detect the presence of specific biomolecules. A cavity near the gate impacts the oxide capacitance of the device, and this, in turn, impacts the different device characteristics like the drain current, transconductance, and threshold voltage of the device. The novelty of this work is the proposal of a quad-cavity double-gate tapered dielectric MOSHEMT proposed for biosensing applications. The tapered dielectric offers more binding surface for the biomolecules in the cavity. The proposed device is compared with its counterpart, conventional MOSHEMT biosensors. A tapered dielectric component offers increased area for biomolecule binding than its non-tapered counterpart. The increased number of cavity under the gate (CUG; quad CUG) structures allows more biomolecule binding sites under the gate, hence increased parameter variation probability. This article is subdivided into the following sections: Section 2 presents the device structure; Section 3 presents the sensitivity analysis of a quad cavity tapered dielectric of a double-gate MOSHEMT; Section 4 presents results and discussion; and conclusions are provided in Section 5.

2 Device structure

A double-gate MOSHEMT features two gate electrodes on a thin semiconductor layer, forming a dual-gate structure. The thin semiconductor layer is typically composed of a high-mobility material, as seen in Figure 1a. The gates are separated by a nanometer-scale thickness, allowing for precise control of the channel's charge density. These devices operate based on charge modulation in the channel region between the two gates by applying different voltages to the two gates, which enables enhanced gate control over the device, leading to improved performance compared to traditional single-gate transistors. The experiment used a double-gate MOSHEMT (DG-MH) with a $100\,nm$ gate length, with a $10\,nm$ HfO_2 as the insulator material under each gate, having two $18\,nm$ ternary AlGaN as the barrier confining a binary III-V compound $180\,nm$ GaN as the channel. The models used for simulation were calibrated with the results of the literature [18], as presented in Figure 1b. The calibration was obtained with a root mean square (RMS) value of 0.078, and the average % deviation between the values is calculated to be 2.6%.

Using a Cogenda Visual TCAD 2D simulator, we analyzed the performance of a double-gate tapered dielectric AlGaN/GaN MOSHEMT with a quad cavity under the gate toward potential biosensing applications.

Keeping the device dimensions similar, a cavity under the gate (CUG) was incorporated in the DG-MH to explore the device's applicability toward biosensing applications. Figure 2 presents the cross-section of the proposed AlGaN/GaN double-gate double-CUG-MOSHEMT (DG-DCUG-MH) and double-gate quad cavity under the gate tapered dielectric MOSHEMT (DG-QC-TD-MH) (DG-QCUG-TD-MH). The device has a double gate of aluminum with length $\left(L_g\right)$ of $100\,nm$, respectively. The top and bottom oxides each have a thickness $\left(h_{ox}\right)$ of $10\,nm$. The DG-DCUG-MH has two CUGs ($CUG_1\,and\,CUG_2$), while the DG-QCUG-TD-MH has four CUGs ($CUG_{tl}, CUG_{tr}, CUG_{bl}, and\,CUG_{br}$). The length of each CUG in DG-DCUG-MH is 50 nm. The DG-QCUG-TD-MH is composed

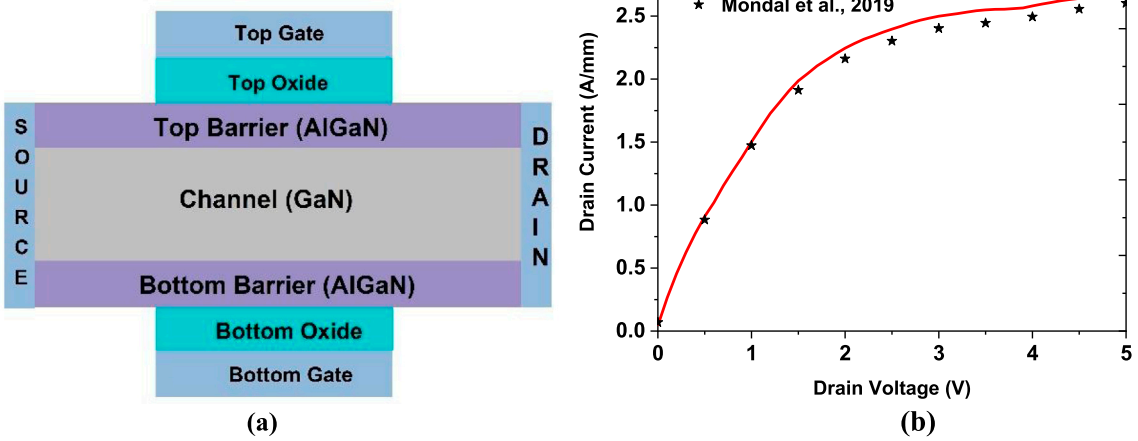

FIGURE 1
(a) Cross section of the double-gate MOSHEMT. **(b)** Simulation model calibration.

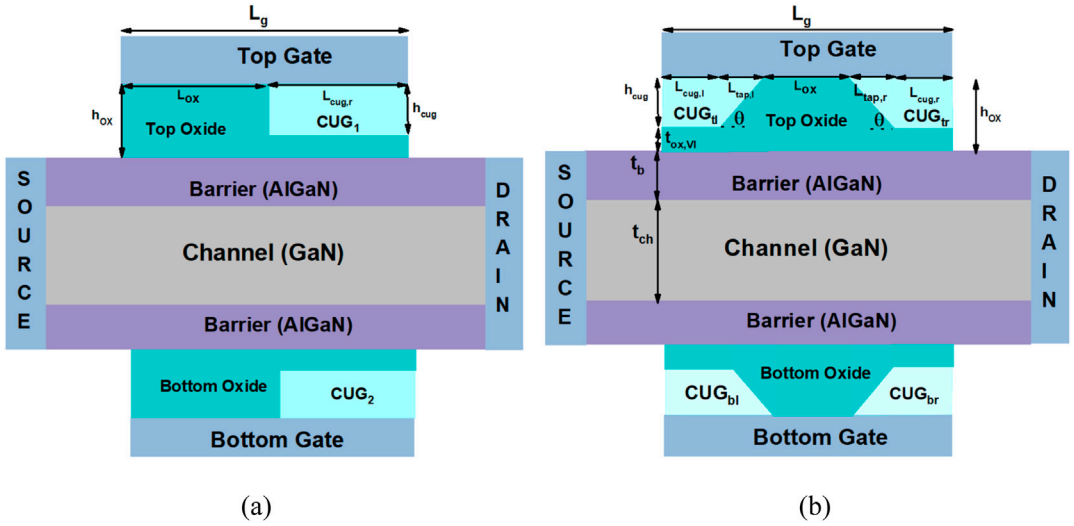

FIGURE 2
Cross section of the **(a)** DG-DuCUG-MH and **(b)** DG-QCUG-TD-MH.

of a tapered ($L_{tap,l}$ and $L_{tap,r}$) and a non-tapered ($L_{cug,l}$ and $L_{cug,r}$) section, as mentioned in Table 1. Each cavity has a height (h_{cug}) of 8 *nm* in the current investigation. Two $Al_xGa_{1-x}N$ barriers with an Al mole fraction ($x = 0.31$) have been considered with a thickness (t_b) of 18 *nm* [18] over the GaN channel with thickness t_{ch}. The source and drain form ohmic-type contacts.

Biomolecules have different shapes and are associated with different dielectric constants. The DG-QCUG-TD-MH can act as a biosensor if we modulate the dielectric constants of the CUG regions to emulate the presence of neutral biomolecules. Any surface modification near the gate affects the 2DEG of the MOSHEMT and can be used to study the variation in parameters due to the presence of biomolecules that can be further used to perform the sensitivity analysis. Possible fabrication steps of a tapered cavity were presented in our previous work [35, 36]. Because 20° tapered cavities have been fabricated [37] with precise photolithography and meticulous etching, a 60° tapered CUG may also be feasible. However, fabrication of these nanocavities comes with different fabrication challenges. Process variability can significantly impact achieving consistent nanometer-scale dimensions and the desired tapered geometry, thereby affecting the performance of the biosensor. Both the fabrication process and the subsequent bioassay functionalization can result in surface roughness, which can affect the performance. High-resolution techniques like electron beam lithography and focused ion beam milling are expensive and slow, limiting their use for mass production. Integrating the tapered nanostructures into a complete, functional biosensor system requires complex multi-step processes.

TABLE 1 Device dimensions.

Layer	Dimension
Top oxide, bottom oxide, h_{ox}	10 nm
Barrier, t_b	22 nm
Channel, t_{ch}	180 nm
Length of top and bottom gates, L_g	100 nm
Length of non-tapered oxide, L_{ox}	24 nm (DG-QCUG-TD-MH) 50 nm (DG-DCUG-MH)
Length of non-tapered CUG, L_{cug}	30 nm (DG-QCUG-TD-MH) 50 nm (DG-DCUG-MH)
Length of tapered section, L_{tap}	8 nm
Height of cavity, h_{cug}	8 nm

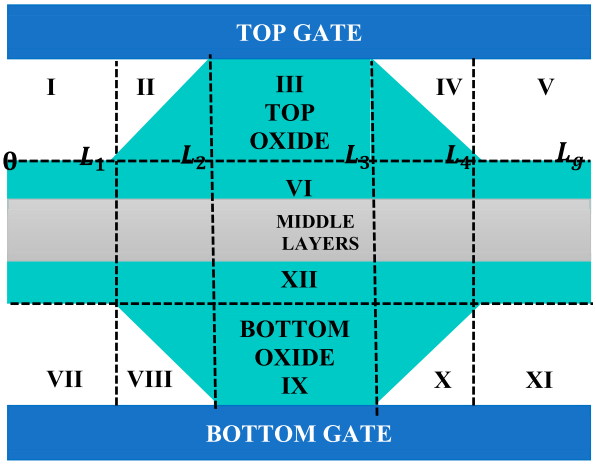

FIGURE 3
Enlarged under the gate region.

3 Sensitivity analysis of a DG-QCUG-TD-MH

The top gate section is shown in Figure 3. The capacitance in each region is calculated as follows. The middle layers constitute the top and bottom barrier layers and the channel.

The gate region is subdivided as follows:

$$Region\ I, VII: 0 < x < L_1, 0 < y < h_{cug},$$

$$Region\ II, VIII: L1 < x < L2, 0 < y < h_{cug},$$

$$Region\ III, IX: L2 < x < L3, 0 < y < t_{ox,III},$$

$$Region\ IV, X: L3 < x < L4, 0 < y < h_{cug},$$

$$Region\ V, XI: L4 < x < Lg, 0 < y < h_{cug},$$

$$Region\ VI, XII: 0 < x < Lg, h_{cug} < y < t_{ox,VI}.$$

Assuming that the CUGs are fully filled, the capacitance of each region can be calculated as follows:

$$C_{I,top} = C_{I,bot} = \epsilon_0 \kappa_{cug} \left\{ \frac{AL_1}{h_{cug} L_g} \right\}, \tag{1a}$$

$$C_{II,top} = C_{II,bot} = \epsilon_0 \kappa_{ox} \kappa_{cug} \left\{ \frac{A(L_2 - L_1)}{h_{cug} L_g (\kappa_{cug} - \kappa_{ox})} \right\} \left\{ \ln \left(\frac{\kappa_{cug}}{\kappa_{ox}} \right) \right\}, \tag{1b}$$

$$C_{III,top} = C_{III,bot} = \epsilon_0 \kappa_{ox} \left\{ \frac{A(L_3 - L_2)}{t_{ox,III} L_g} \right\}, \tag{1c}$$

$$C_{IV,top} = C_{IV,bot} = \epsilon_0 \kappa_{ox} \kappa_{cug} \left\{ \frac{A(L_4 - L_3)}{h_{cug} L_g (\kappa_{ox} - \kappa_{cug})} \right\} \left\{ \ln \left(\frac{\kappa_{ox}}{\kappa_{cug}} \right) \right\}, \tag{1d}$$

$$C_{V,top} = C_{V,bot} = \epsilon_0 \kappa_{cug} \left\{ \frac{A(L_g - L_4)}{h_{cug} L_g} \right\}, \tag{1e}$$

$$C_{VI,top} = C_{VI,bot} = \epsilon_0 \kappa_{ox} \left\{ \frac{A}{t_{ox,VI}} \right\}. \tag{1f}$$

Here, ϵ_0 is the permittivity of free space, κ_{cug} is the relative permittivity of the oxide, A is the gate area, L_g is gate length, and W is the channel width. L_1, L_2, L_3, L_4 are sections of the gate length, h_{cug} is the height of the CUG, and $t_{ox,III}$ and $t_{ox,VI}$ are the thicknesses of the oxide in region III and region VI.

The total capacitance associated with Regions I–V ($C_{ox,I-V}$) is calculated as

$$C_{ox,I-V,top} = C_{ox,I-V,bot} = \sum_{i=I}^{V} C_i. \tag{2}$$

Using Equation 2, the total oxide capacitance ($C_{ox,Tot,top}$) is expressed as

$$C_{ox,Tot,top} = C_{ox,Tot,bot} = \left[\frac{1}{C_{ox,I-V,top}} + \frac{1}{C_{VI,top}} \right]^{-1}. \tag{3}$$

The MOSHEMT capacitance for the top region is assumed to be equal to the capacitance of the bottom region which is expressed in Equation 3 as

$$C_{MOSHEMT,top} = C_{MOSHEMT,bot} = \frac{C_b, C_{ox,Tot,top}}{C_{ox,Tot,top} + C_b}, \tag{4}$$

where A stands for the area of the individual region, and $C_{b,top} = C_{b,bot} = \frac{\epsilon_0 \epsilon_b}{t_b}$ are the capacitances of the barrier layers. Here, ϵ_b is the relative permittivity of the barrier layers, and t_b specifies the thickness of the barrier layers, in Equations 3, 4, the subscript on the right-hand side may be replaced by to depict the capacitance of the bottom layer.

The capacitance terms $C_{MOSHEMT,top}$ and $C_{MOSHEMT,bot}$ are connected in series, so the total MOSHEMT capacitance ($C_{MOSHEMT,Tot}$) can be expressed as

$$C_{MOSHEMT,Tot} = \frac{C_{MOSHEMT,top} C_{MOSHEMT,bot}}{C_{MOSHEMT,top} + C_{MOSHEMT,bot}}. \tag{5}$$

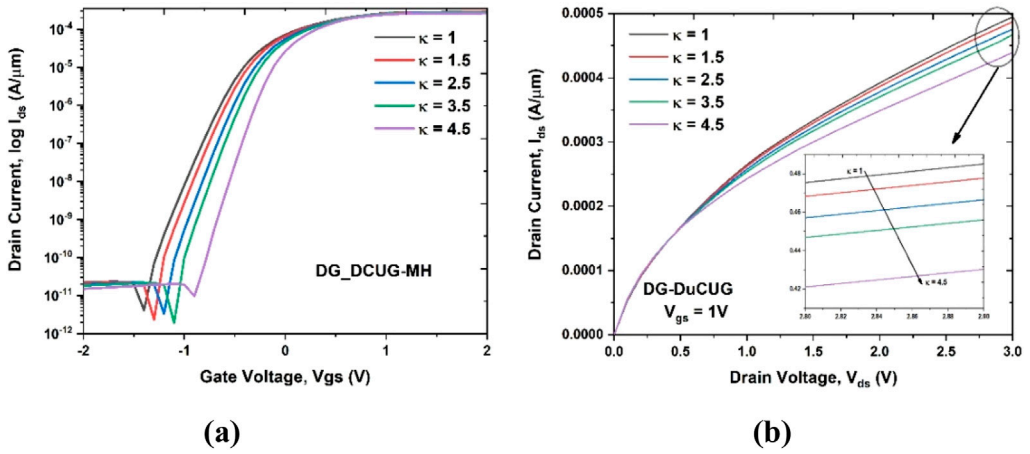

FIGURE 4
(a) I_d–V_g and **(b)** I_d–V_d characteristics of the DG-DCUG-MH.

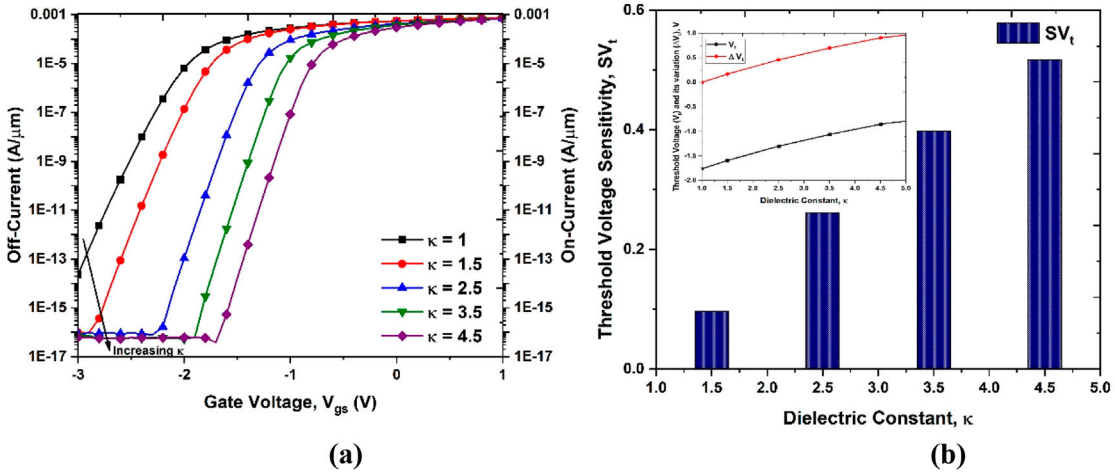

FIGURE 5
(a) I_d–V_g characteristics and **(b)** sensing metrics V_t of the DG-QCUG-TD-MH k values.

The MOSHEMT capacitance derived in Equation 5 are used to perform the sensitivity analysis, as it impacts the drain current, which in turn affects other parameters like transconductance and output conductance. The presence of a neutral biomolecule in the CUG will change the surface potential, which impacts the sheet carrier density and therefore the drain current. The sensitivity analysis uses Equation 6 to determine the variations in the different sensing parameters (P), such as the on current (I_{ON}), off current (I_{OFF}), threshold voltage (V_t), transconductance (g_m), drain current (I_{ds}), and output conductance (g_{ds}) both when the CUG has no molecule and when biomolecules enter the CUG [17].

$$S_P = \left| \frac{\Delta P}{P^{NM}} \right|, \tag{6}$$

where $\Delta P = \left| P^{NM} - P^{BM} \right|$, S_P represents sensitivity, ΔP represents the difference in the sensing parameters due to the biomolecule hybridization in the cavity, P^{NM} is the sensing parameter of the device with no molecule (NM) in the CUG, and P^{BM} is the sensing parameter of the device with a biomolecule (BM) in the cavity (neutral). The sensitivity analysis is based on the variation of the parameters of the device due to the presence of biomolecules rather than the value of the variation.

4 Results and discussion

This section is divided into three sub-sections. The first sub-section discusses the sensing metrics for a DG-DCUG-MH, while the next sub-section delves into different studies for the DG-QCUG-TD-MH. The last part of this section makes a comparison between different MOSHEMT structures with tapered and non-tapered dielectric with single to quad CUG structures.

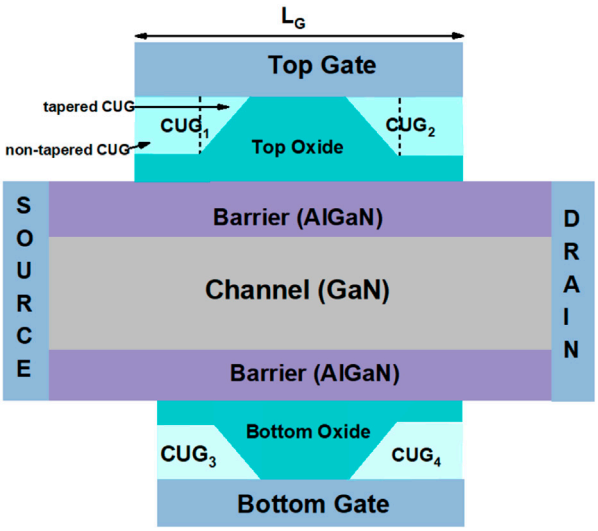

FIGURE 6
DG-QCUG-TD-MH showing the four CUGs, each having two sections (tapered and non-tapered).

4.1 DG-DCUG-MH

This section presents the sensitivity analysis of the structure presented in Figure 2a. Here, we have considered that both the CUGs are 100% full.

Figure 4a shows the I_{ON} and I_{OFF} and the drain characteristics of the DG-DCUG AlGaN/GaN MOSHEMT, where, when the CUG is not filled with any biomolecule, the $\frac{I_{ON}}{I_{OFF}}$ is found to be $\sim 10^{10}$, which improves to $\sim 10^{11}$ when the CUGs are filled with biomolecules. The I_{OFF} reduced as κ increases, thereby improving leakage performance. As κ increases, it enhances gate-to-channel capacitive coupling, allowing the gate to more effectively suppress channel conduction at low gate bias. Because the OFF-state current is dominated by leakage mechanisms, the enhanced electrostatic screening and gate control associated with higher κ values lead to a systematic reduction in I_{OFF}. Figure 4b shows improvement in drain current with dielectric constant κ, which is attributed to enhanced gate-to-channel capacitive coupling, which increases the 2DEG density and channel conductivity for a given gate bias. The numerical results are presented in Table 6.

4.2 DG-QCUG-TD-MH

4.2.1 Impact of κ on sensing metrics

This section presents the sensitivity analysis of the structure presented in Figure 2b. Here, we have considered the effect of neutral biomolecules, angle of taper, and fill percentage on the sensing metrics.

The dielectric constant of the CUG sections under the gate is modulated between (1-4.5) to study its impact on various device parameters.

Figure 5a shows the I_{ON} and I_{OFF} of the tapered dielectric double-gate AlGaN/GaN MOSHEMT. When the CUG is not filled with any biomolecule, the $\frac{I_{ON}}{I_{OFF}}$ is found to be 10^{13} and improves to 10^{17} when the CUGs are filled with biomolecules. The I_{OFF} is reduced as κ increases, thereby improving leakage performance. As in DG-DCUG-MH, here also the I_{OFF} is reduced as κ increases, thereby improving leakage performance in both structures. This structure offers an improved sensitivity compared to the previous structure. Figure 5b shows that the threshold voltage sensitivity of the DG-QCUG-TD-MH improves with κ. The observed improvement in threshold voltage with increasing dielectric constant κ arises from enhanced gate-to-channel capacitive coupling, which enables earlier 2DEG formation and stronger channel band bending at reduced gate bias. The threshold

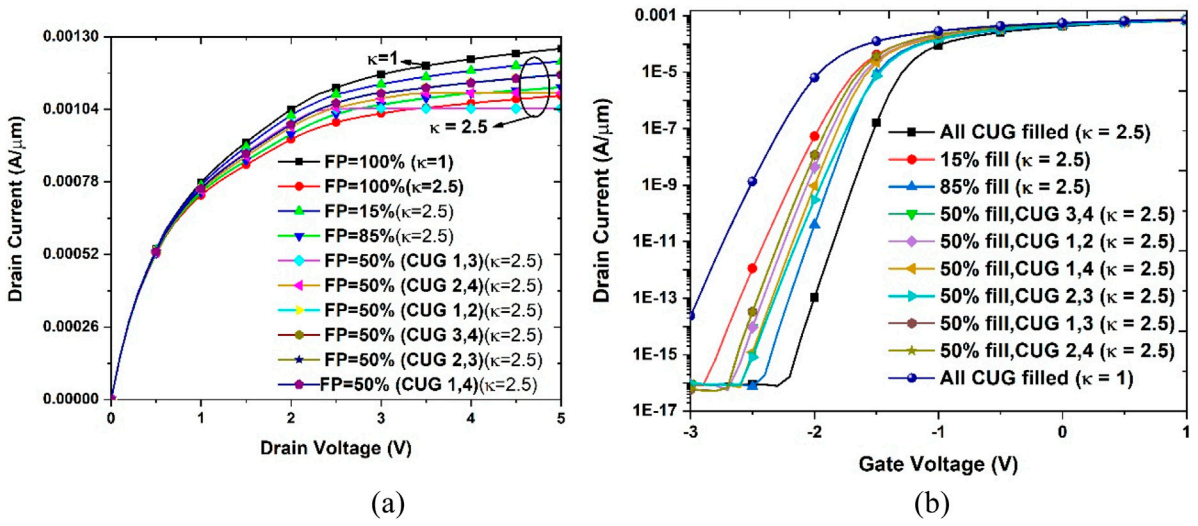

FIGURE 7
(a) I_d–V_d for different fill percentages (FPs) with κ = 2.5. **(b)** I_d–V_g for different fill percentages with κ = 2.5.

TABLE 2 Fill % results of DG-QCUG-TD-MH on I_{ON}/I_{OFF}.

Fill percent (θ = 60°)	k	I_{ON}	I_{OFF}	I_{ON}/I_{OFF}
100%	1	$7.25X10^{-4}$	$2.31X10^{-14}$	$3.14X10^{10}$
	2.5	$6.83X10^{-4}$	$8.69X10^{-17}$	$7.86X10^{12}$
85%		$6.91X10^{-4}$	$9.03X10^{-17}$	$7.65X10^{12}$
50% (CUG 1,2)		$7.04X10^{-4}$	$9.00X10^{-17}$	$7.82X10^{12}$
50% (CUG 3,4)		$7.05X10^{-4}$	$9.11X10^{-17}$	$7.74X10^{12}$
50% (CUG 1,4)		$6.71X10^{-4}$	$8.68X10^{-17}$	$7.73X10^{12}$
50% (CUG 2,3)		$6.99X10^{-4}$	$9.55X10^{-17}$	$7.72X10^{12}$
50% (CUG 1,3)		$7.56X10^{-4}$	$6.37X10^{-17}$	$1.19X10^{13}$
50% (CUG 2,4)		$7.56X10^{-4}$	$5.71X10^{-17}$	$1.32X10^{13}$
15%		$7.14X10^{-4}$	$8.53X10^{-17}$	$8.37X10^{12}$

voltage in this analysis was obtained by the constant-current method. The results are shown in Table 6.

4.2.2 Impact of different fill percentages on sensing metrics

To study the impact of incomplete biomolecule immobilization in the CUG, different fill percentages were considered for the device with a $\theta = 60°$ angle of taper and oxide height $y = 0$ to $y = h$ and $x = 0$ to $= L_G$. Each CUG, as well as the oxide region, is considered to have two parts: a tapered part ($tapcug_i$ and $tapox_i$) and a non-tapered part ($ntapcug_i$ and $ntapox_i$), where i denotes the CUG and oxide number 1 to 4, as shown in Figure 6. The larger taper angle (60°) results in an enhanced electric field near the CUG and at the cavity–channel interfaces, which strengthens the gate-to-channel capacitive coupling and improves modulation of the two-dimensional electron gas in response to dielectric or charge perturbations introduced by biomolecules in the CUG. As a result, the sensitivity enhancement arises from nonlinear electrostatic effects rather than purely geometric scaling. Moreover, the combination of a large-angle tapered cavity with a quad-cavity, double-gate configuration introduces multiple high-field interaction regions along the channel, leading to cumulative and symmetric channel potential modulation.

A 100% fill is obtained by considering that the neutral biomolecules have occupied the entire CUG space (CUG_{1-4}). An 85% fill is obtained by considering that only the non-tapered part of each CUG is filled with biomolecules. A 50% fill percent was analyzed by considering a different combination of CUGs to be fully filled, like only the top CUGs (CUG_1, CUG_2), only the bottom CUGs (CUG_3, CUG_4), or only the left CUGs (CUG_1, CUG_4), and so on. A 15% fill is represented by filling only the tapered portion of each CUG ($tapered\,cug_{1-4}$).

Figure 7a shows the change in drain current for different fill percentages. Figure 7b is used to extract the $\frac{I_{ON}}{I_{OFF}}$ for different fill percentages for a taper angle of 60°. The values are shown in Tables 2,3.

Table 2 and Table 3 show the I_{ON}/I_{OFF}, $|\Delta I_{ds}|$, and $|\Delta g_m|$ values for different fill percentages for a taper angle 60°, respectively. When the drain-side CUG is filled slightly, better I_{OFF} is obtained. The highest I_{ON}/I_{OFF} is obtained when the drain-side CUG is filled because the high-κ cavity strongly screens drain-induced electric fields, significantly reducing OFF-state leakage while leaving ON-state source injection largely unaffected. The negligible change in the I_D-V_{DS} characteristics arises because the structural modification primarily suppresses drain-induced leakage mechanisms, while the ON-state current, which is dominated by source-side injection and velocity saturation, remains unchanged. The device I_{ds} is compared with existing literature, which reported a value of 1.23 mA/μm [27], $1.1mA/\mu m$ for a ($2nm$) HfO_2 DG MOSHEMT [28]. The

TABLE 3 Effect of fill % of DG-QCUG-TD-MH on $|\Delta I_{ds}|$ and $|\Delta g_m|$.

Fill Percent ($\theta = 60°$)	κ	$I_{ds}\|_{Vds=constant}$	$\|\Delta I_{ds}\|$	g_m	$\|\Delta g_m\|$
100%	1	$8.21X10^{-4}$	–	$3.29X10^{-4}$	–
	2.5	$8.36X10^{-4}$	$0.15X10^{-4}$	$3.48X10^{-4}$	$0.19X10^{-4}$
85%		$8.34X10^{-4}$	$0.13X10^{-4}$	$3.19X10^{-4}$	$0.1X10^{-4}$
50% (*CUG* 1,2)		$8.28X10^{-4}$	$0.7X10^{-4}$	$3.50X10^{-4}$	$0.21X10^{-4}$
50% (*CUG* 3,4)		$8.29X10^{-4}$	$0.8X10^{-4}$	$3.47X10^{-4}$	$0.18X10^{-4}$
50% (*CUG* 1,4)		$8.29X10^{-4}$	$0.8X10^{-4}$	$3.35X10^{-4}$	$0.06X10^{-4}$
50% (*CUG* 2,3)		$8.27X10^{-4}$	$0.6X10^{-4}$	$3.58X10^{-4}$	$0.29X10^{-4}$
50% (*CUG* 1,3)		$9.25X10^{-4}$	$1.04X10^{-4}$	$3.79X10^{-4}$	$0.5X10^{-4}$
50% (*CUG* 2,4)		$9.25X10^{-4}$	$1.04X10^{-4}$	$3.78X10^{-4}$	$0.49X10^{-4}$
15%		$8.22X10^{-4}$	$0.01X10^{-4}$	$3.50X10^{-4}$	$0.21X10^{-4}$

10.3389/fphy.2025.1732657

TABLE 4 Sensing area and angle of taper calculation.

$L_{topox,i} = L_{tapcug,i}(nm)$	$h_i(nm)$	$L_{ntapcug,i}(nm)$	$L_{ntapox}(nm)$	Area of non-tapered section + area of tapered section = area of CUG_i	Angle of taper of CUG_i, θ
15	4	5	60	20 + 30 = 50	15°
12	8	8		64 + 48 = 112	30°
8	8	12		96 + 32 = 128	45°
5	8	15		120 + 20 = 140	60°

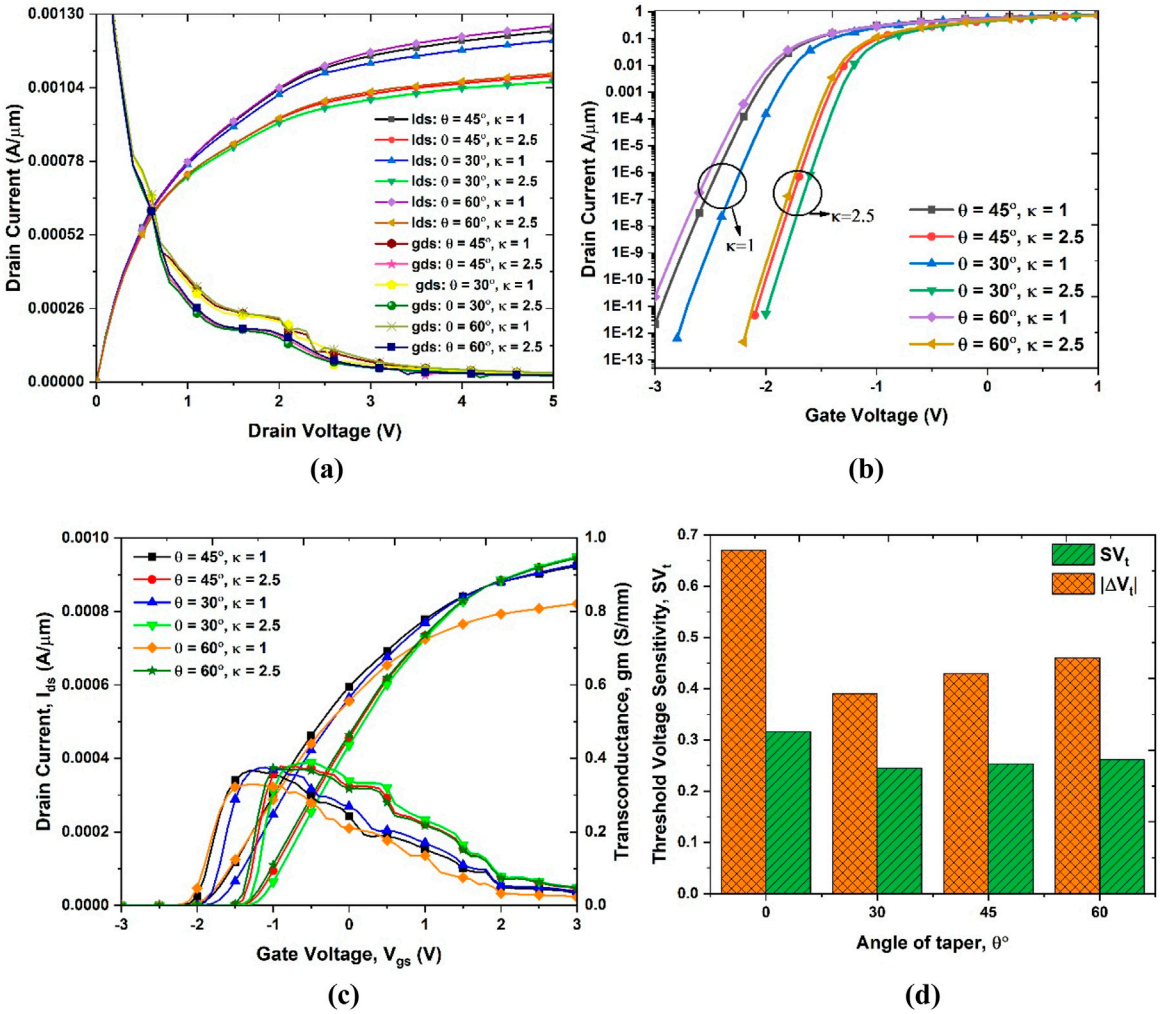

FIGURE 8
Sensing metrics for different taper angles κ = 2.5. **(a)** I_d–V_d, **(b)** I_{ON} and I_{OFF}, **(c)** I_d–V_g and g_m, and **(d)** V_t.

higher transconductance observed when the source-side cavity is filled originates from enhanced gate control over the source injection barrier and increased sensitivity of the 2DEG density to gate voltage variations, amplified by the electric field in the tapered geometry.

The I_{ds}, $\frac{I_{ON}}{I_{OFF}}$, and V_t values can be affected by variations in the presence of the target biomolecules or analytes. A higher variation in the $\frac{I_{ON}}{I_{OFF}}$ ratio suggests that even small concentrations of the target biomolecules can be detected with a significant change in the electrical signal.

TABLE 5 I_{ON}/I_{OFF} values for different taper angles.

The angle of taper, θ (Fill 100 %)	κ	I_{ON}	I_{OFF}	$\frac{I_{ON}}{I_{OFF}}$
0°	1	$7.96X10^{-4}$	$2.31X10^{-14}$	$3.45X10^{10}$
0°	2.5	$7.43X10^{-4}$	$1.66X10^{-14}$	$4.47X10^{10}$
30°	1	$7.69X10^{-4}$	$5.6X10^{-13}$	$1.37X10^{9}$
30°	2.5	$7.26X10^{-4}$	$5.02X10^{-12}$	$1.45X10^{8}$
45°	1	$7.78X10^{-4}$	$6.02X10^{-12}$	$1.29X10^{8}$
45°	2.5	$7.33X10^{-4}$	$5.20X10^{-12}$	$1.41X10^{8}$
60°	1	$7.25X10^{-4}$	$8.20X10^{-11}$	$0.88X10^{7}$
60°	2.5	$7.36X10^{-4}$	$6.58X10^{-11}$	$1.12X10^{7}$

4.2.3 Impact of different angles of taper on sensing metrics

The sites available for biomolecule hybridization are a critical parameter for sensitivity analysis. The area of one CUG section can be modulated by changing the angle of taper. Table 4 presents the calculations for the sensing area and the angle of the taper by adjusting the CUG dimensions as shown.

Sensitivity to threshold voltage variations impacts how well the transistor turns on and off. These metrics are crucial for achieving low limits of detection and accurate quantification. The angle of the taper is modified by modulating the length and height of the tapered sections. The slope dielectric layer could impact the device's electrical characteristics, as it modifies the hybridization section of the CUG. The angle of the taper can influence various device characteristics of the MOSHEMT, such as threshold voltage, transconductance, and leakage performance. These characteristics collectively determine the device's operational performance in different applications. Figure 8 presents the variation and thereby the sensitivity of the drain current, on-off current ratio, transconductance, and threshold voltage. The variation in threshold voltage improves as the angle of taper is increased to 60°, suggesting that as tapering increases the sensing area, sensitivity is improved. The $\frac{I_{ON}}{I_{OFF}}$ reported in a double-gate MOSHEMT [27] is 290. Our results show improved results over the reported literature. Table 5 presents the $\frac{I_{ON}}{I_{OFF}}$ values for different taper angles, which are observed to decrease with increase in θ. The decrease in $\frac{I_{ON}}{I_{OFF}}$ with increasing taper angle θ occurs because ON-state current enhancement saturates at larger θ, while the OFF-state leakage increases due to stronger lateral electric-field crowding and enhanced drain-induced barrier lowering.

4.3 Comparison of different MOSHEMT structures

Table 6 shows a comparison between the different structures implemented by the authors in previous works and this work. Every structure shows variation in some parameters when the permittivity of the CUG changes. The single-gate, single-CUG MOSHEMT (SG-SCUG-MH) is implemented in [17], the single-gate, dual-CUG-MOSHEMT (SG-DuCUG-MH) is implemented in [38], the single-gate, single-CUG tapered dielectric MOSHEMT

TABLE 6 Comparison of parameter variations for different MOSHEMT structures.

Device type	SG-SCUG-MH [17]	SG-SCUG-TD-MH [35]	SG-DuCUG-MH [38]	SG-DCUG-TD-MH [36]	DG-DCUG-MH [this work]	DG-QC-TD-MH [this work]
$\Delta I_{ds}\left(\frac{mA}{mm}\right)$	319.0	24.4	404	170	55.2	160
$S_{I_{ds}}$	0.32	0.34	0.52	0.62	0.11	0.69
$\Delta I_{ON}\left(\frac{mA}{mm}\right)$	330.3	125	366	157	220	147
$S_{I_{ON}}$	0.39	0.53	0.62	1.35	0.08	0.65
$\Delta I_{OFF}\left(\frac{A}{\mu m}\right)$	$12n$	$29n$	$38.6n$	$96n$	$4.69p$	$125f$
$S_{I_{OFF}}$	0.41	0.48	0.64	0.80	0.07	0.99
ΔV_t (V)	0.28	0.31	0.04	0.35	0.16	1.67
S_{V_t}	0.22	0.47	0.92	0.89	0.88	0.95
$\Delta g_m\left(\frac{mS}{mm}\right)$	102.0	61.3	449	225	62.3	11
S_{g_m}	0.73	0.88	1.05	1.28	0.28	0.29
$\Delta g_{ds}\left(\frac{mS}{mm}\right)$	534.9	571	1013	407	31.0	7.7
$S_{g_{ds}}$	0.52	0.61	0.68	0.76	0.06	0.24

TABLE 7 Comparison of parameter and sensitivity variations with existing biosensors.

Device type	MOSHEMT [39]	MOSHEMT [40]	MOSHEMT [41]	MOSFET [42]	DG-QC-TD-MH [this Work]
$\Delta I_{ds}\left(\frac{mA}{mm}\right)$	—	125.32	40.99	—	160
$S_{I_{ds}}$	0.024	—	0.3937	0.531	0.69
ΔV_t (V)	—	1.42	−3.45	—	1.67
S_{V_t}	0.068	—	0.2247	—	0.95

(SG-SCUG-TD-MH) is implemented in [35], and the single-gate, dual-CUG MOSHEMT (SG-SCUG-MH) is implemented in [37]. The table shows that the tapered shows better sensitivity over its non-tapered counterpart. The comparison was carried out for $\kappa = 8$.

For all cases, the DG-QC-TD-MH exhibits an improved sensitivity over the other structures. Each structure can detect a biomolecule when a suitable sensing metric is selected. A comparison of the single-gate and double-gate structures shows that the latter give better results, but this is at the cost of fabrication complexities and the impact of short-channel effects as the gate length was reduced for double-gate structures. The single-gate structures with single and dual CUG with non-tapered and tapered dielectric using HfO_2 gave reasonably better results than the existing literature. We see an improvement in sensitivity in the tapered dielectric structures, ranging from single to double gates, owing to the increased sensing area and hybridization section made available in the CUG.

Table 7 presents a comparison of variation in parameters and sensitivity with recent MOSHEMT and MOSFET biosensors. Note that the proposed DG-QC-TD-MH structure offers higher sensitivity than its counterparts. The improved sensitivity values are due to the larger surface area offered by the tapered cavities under the gate.

5 Conclusion

This article delves into the applicability of double-gate structures for biosensing. To analyze the performance of the device in the nano regime, a gate length of 100 nm is used to obtain improved results for various metrics. Below 50 nm, as L_g shrinks, the source and drain depletion regions begin to overlap, weakening gate control. SCE performance degrades, and DIBL and SS increase. A DG-MH structure with a CUG as a biosensor leverages the benefits of a double-gate structure and the high electron mobility properties of the semiconductor material to achieve sensitive and accurate biomolecule detection. The compact nature of the double-gate design allows for miniaturization, making it suitable for portable and point-of-care diagnostic applications.

Data availability statement

The original contributions presented in the study are included in the article/supplementary material; further inquiries can be directed to the corresponding author.

Author contributions

AD: Formal analysis, Writing – original draft. NA: Data curation, Methodology, Writing – review and editing. TP: Supervision, Methodology, Writing – original draft. SM: Validation, Writing – review and editing. KP: Writing – review and editing. GK: Writing – review and editing.

Funding

The author(s) declared that financial support was received for this work and/or its publication. This work was supported and funded by the Deanship of Scientific Research at Imam Mohammad Ibn Saud Islamic University (IMSIU) (grant number IMSIU-DDRSP2603).

Conflict of interest

The author(s) declared that this work was conducted in the absence of any commercial or financial relationships that could be construed as a potential conflict of interest.

Generative AI statement

The author(s) declared that generative AI was not used in the creation of this manuscript.

Any alternative text (alt text) provided alongside figures in this article has been generated by Frontiers with the support of artificial intelligence and reasonable efforts have been made to ensure accuracy, including review by the authors wherever possible. If you identify any issues, please contact us.

Publisher's note

References

1. Mishra SN, Jena K. A dielectric-modulated normally-off AlGaN/GaN MOSHEMT for bio-sensing application: analytical modeling study and sensitivity analysis. *J Korean Phys Soc* (2019) 74(4):349–57. doi:10.3938/jkps.74.349

2. Varghese A, Periasamy C, Bhargava L. Fabrication and charge deduction based sensitivity analysis of GaN MOS-HEMT device for glucose, MIG, C-erbB-2, KIM-1, and PSA detection. *IEEE Trans Nanotechnol* (2019) 18:747–55. doi:10.1109/tnano.2019.2928308

3. Sarangadharan I, Pulikkathodi AK, Chu CH, Chen YW, Regmi A, Chen PC, et al. Review—high field modulated FET biosensors for biomedical applications. *ECS J Solid State Sci Technol* (2018) 7(7):Q3032–Q3042. doi:10.1149/2.0061807jss

4. Syu Y-C, Hsu W-E, Lin C-T. Review field effect transistor biosensing: devices and clinical applications. *ECS J Solid State Sci Technol* (2018) 7(7):Q3196–Q3207. doi:10.1149/2.0291807jss

5. Hemaja V, Panda DK. A comprehensive review on high electron mobility transistor (HEMT) based biosensors: recent advances and future prospects and its comparison with Si-Based biosensor. *Silicon* (2021) 14:1873–86. doi:10.1007/s12633-020-00937-w

6. Djelti H. The DC behavior of the Al0.25Ga0.75N/GaN MOS-HEMT. In: *Proceedings of 2016 international renewable and sustainable energy conference, IRSEC 2016* (2017). p. 657–60. doi:10.1109/IRSEC.2016.7984009

7. Poonia R, Bhat AM, Periasamy C, Sahu C. Performance analysis of MOS-HEMT as a biosensor: a dielectric modulation approach. *Silicon* (2022) 14(15):10023–36. doi:10.1007/S12633-022-01742-3/METRICS

8. Pal P, Pratap Y, Gupta M, Kabra S. Modeling and simulation of AlGaN/GaN MOS-HEMT for biosensor applications. *IEEE Sens J* (2019) 19(2):587–93. doi:10.1109/JSEN.2018.2878243

9. Bhat AM, Varghese A, Shafi N, Periasamy C. A dielectrically modulated gaN/alN/alGaN MOSHEMT with a nanogap embedded cavity for biosensing applications. *IETE J Res* (2021) 69:1419–28. doi:10.1080/03772063.2020.1869593

10. Varghese A, Periasamy C, Bhargava L, Bin Dolmanan S, Tripathy S. Linear and Circular AlGaN/AlN/GaN MOS-HEMT-based pH Sensor on Si Substrate: a Comparative Analysis. *IEEE Sensors Lett* (2019) 3(4):2019–22. doi:10.1109/LSENS.2019.2909291

11. Shaveta HMMA, Chaujar R. Rapid detection of biomolecules in a dielectric modulated GaN MOSHEMT. *J Mater Sci Mater Electron* (2020) 31(19):16609–15. doi:10.1007/s10854-020-04216-7

12. Pal P, Pratap Y, Gupta M, Kabra S. Analytical modeling and simulation of AlGaN/GaN MOS-HEMT for high sensitive pH sensor. *IEEE Sens J* (2021) 21(12):12998–3005. doi:10.1109/JSEN.2021.3069243

13. Jena K, Swain R, Lenka TR. Effect of thin gate dielectrics on DC, radio frequency and linearity characteristics of lattice-matched alInN/alN/gaN metal-oxide-semiconductor high electron mobility transistor. *IET Circuits, Devices Syst* (2016) 10(5):423–32. doi:10.1049/iet-cds.2015.0332

14. Kiran G, Krishna R, Dwivedi P, Sharma P, Singh R. Analytical modeling of MgZnO/ZnO MOSHEMT based biosensor for biomolecule detection. *Superlattices Microstruct.* (2022) 163:107130. doi:10.1016/J.SPMI.2021.107130

15. Varghese A, Periasamy C, Bhargava L, Bin Dolmanan S, Tripathy S. Fabrication and modeling-based performance analysis of circular GaN MOSHEMT-based electrochemical sensors. *IEEE Sens J* (2021) 21(4):4216–24. doi:10.1109/JSEN.2020.3032175

16. Varghese A, Das P, Tallur S. A complete analytical model for MOS-HEMT biosensors: capturing the effect of Stern layer and charge screening on sensor performance. *IEEE Sensors Lett* (2021) 1472(AUGUST 2020):1–4. doi:10.1109/LSENS.2021.3065509

17. Dastidar A, Patra TK, Mohapatra SK, Braim M, Pandiaraj S, Alshammari A, et al. Sensitivity analysis of Al0.3Ga0.7N/GaN dielectric modulated MOSHEMT biosensor. *ECS J Solid State Sci Technol* (2023) 12(6):067006. doi:10.1149/2162-8777/ACDFF9

18. Mondal A, Roy A, Mitra R, Kundu A. Comparative study of variations in gate oxide material of a novel underlap DG MOS-HEMT for Analog/RF and high power applications. *Silicon* (2020) 12(9):2251–7. doi:10.1007/s12633-019-00316-0

19. Rahman E, Shadman A, Khosru QDM. Effect of biomolecule position and fill in factor on the sensitivity of a dielectric modulated double gate junctionless MOSFET biosensor. *Sens Bio-sens Res* (2017) 13:49–54. doi:10.1016/j.sbsr.2017.02.002

20. Panda DK, Singh R, Lenka TR, Pham TT, Velpula RT, Jain B, et al. Single and double-gate based AlGaN/GaN MOS-HEMTs for the design of low-noise amplifiers: a comparative study. *IET Circuits, Devices Syst* (2020) 14(7):1018–25. doi:10.1049/iet-cds.2020.0015

21. Vasallo BG, Wichmann N, Bollaert S, Roelens Y, Cappy A, Gonzalez T, et al. Comparison between the dynamic performance of double- and single-gate AlInAs/InGaAs HEMTs. *IEEE Trans Electron Devices* (2007) 54(11):2815–22. doi:10.1109/TED.2007.907801

22. Pardeshi H. Analog/RF performance of AlInN/GaN underlap DG MOS-HEMT. *Superlattices Microstruct.* (2015) 88:508–17. doi:10.1016/j.spmi.2015.10.009

23. Rao M, Ranjan R, Kashyap N, Sarin RK. Performance analysis of Normally-on dual gate algan/gan hemt. *Trans Electr Electron Mater* (2021) 22(5):691–9. doi:10.1007/S42341-021-00286-4

24. Vadizadeh M, Fallahnejad M, Shaveisi M, Ejlali R, Bajelan F. Double Gate double-channel AlGaN/GaN MOS HEMT and its applications to LNA with Sub-1 dB noise figure. *Silicon* (2023) 15(2):1093–103. doi:10.1007/s12633-022-02083-x

25. Husna Hamza K, Nirmal D. A review of GaN HEMT broadband power amplifiers. *AEU - Int J Electronics Commun* (2020) 116:153040. doi:10.1016/j.aeue.2019.153040

26. Roy A, Mitra R, Mondal A, Kundu A. Analog/RF and power performance analysis of an underlap DG AlGaN/GaN based High-K dielectric MOS-HEMT. *Silicon* (2022) 14(5):2211–8. doi:10.1007/s12633-021-01020-8

27. Pati SK, Pardeshi H, Raj G, Mohan Kumar N, Sarkar CK. Impact of gate length and barrier thickness on performance of InP/InGaAs based double gate metal-oxide-semiconductor heterostructure field-effect transistor (DG MOS-HFET). *Superlattices Microstruct.* (2013) 55(1):8–15. doi:10.1016/j.spmi.2012.12.002

28. Saravana Kumar R, Poornachandran R, Baskaran S, Mohan Kumar N, Sandhiya S, Shanmugapriya KU. DC and RF characterization of InAs based double Delta doped MOSHEMT device. In: Proc. Int. Conf. 2018 IEEE Electron Device Kolkata Conf. EDKCON (2018). p. 509–12. doi:10.1109/EDKCON.2018.8770418

29. Mukherjee H, Dasgupta R, Kar M, Kundu A. A comparative analysis of analog performances of underlapped dual gate AlGaN/GaN based MOS-HEMT and Schottky-HEMT. In: 2020 IEEE Calcutta Conf. CALCON 2020 - Proc. (2020). p. 412–6. doi:10.1109/CALCON49167.2020.9106420

30. Mitra R, Roy A, Kundu A, Kar M. Impact of AlGaN doping concentration on the Analog/RF performance of a double gate underlap n-AlGaN/GaN MOSHEMT. *3rd Int Symp Devices, Circuits Syst ISDCS 2020 - Proc* (2020) 3–6. doi:10.1109/ISDCS49393.2020.9263012

31. Pardeshi H, Raj G, Pati S, Mohankumar N, Sarkar CK. Influence of barrier thickness on AlInN/GaN underlap DG MOSFET device performance. *Superlattices Microstruct.* (2013) 60:47–59. doi:10.1016/j.spmi.2013.04.015

32. Verma M, Nandi A. Design and analysis of AlGaN/GaN based DG MOSHEMT for high-frequency application. *Trans Electr Electron Mater* (2020) 21(4):427–35. doi:10.1007/s42341-020-00196-x

33. Das R, Chattopadhyay A, Chanda M, Sarkar CK, Bose C. Analytical modeling of sensitivity parameters influenced by practically feasible arrangement of bio-molecules in dielectric modulated FET biosensor. *Silicon* (2021) 1:1–14. doi:10.1007/S12633-021-01617-Z

34. Rahman E, Shadman A, Khosru QDM. Effect of biomolecule position and fill in factor on sensitivity of a dielectric modulated double gate junctionless MOSFET biosensor. *Sens Bio-sensing Res* (2017) 13:49–54. doi:10.101/j.sbsr.2017.02.002

35. Dastidar A, Patra TK. Impact of tapered dielectric on a gallium nitride metal oxide semiconductor high electron mobility transistor (MOSHEMT) towards biosensing applications. *Lect Notes Electr Eng* (2023) 904:175–86. doi:10.1007/978-981-19-2308-1_19

36. Dastidar A, Patra TK, Mohapatra SK, Pradhan KP, Alodhayb AN. Sensitivity estimation of biosensor in a tapered cavity MOSHEMT. *Phys Scr* (2024) 99(5):055017. doi:10.1088/1402-4896/ad37b0

37. Kumar S, Park H, Cho H, Siddique RH, Narasimhan V, Yang D, et al. Overcoming evanescent field decay using 3D-tapered nanocavities for on-chip targeted molecular analysis. *Nat Commun* (2020) 11:2930. doi:10.1038/s41467-020-16813-5

38. Dastidar A, Kumar T, Sushanta P, Mohapatra K, Braim M, Alodhayb AN. Sensing metrics of a dual - cavity single - gate MOSHEMT. *J Korean Phys Soc* (2023) 83:0123456789–498. doi:10.1007/s40042-023-00885-9

39. Hemalatha RG, Kumar MA, Mishra GS, N M, Ismail KBM, Mahalingam S, et al. Design and simulation of advanced boron-doped GaN cap layer on AlGaN/GaN MOSHEMTs for enhanced label-free biosensing applications. *Biomed Microdevices* (2025) 27(2):1–18. doi:10.1007/s10544-025-00746-1

40. Samal S, Barik L, Kumar A, Mishra GP. GaN heterostructure-based MOSHEMT with an embedded cavity for neutral biomolecule detection. *Proc 6th Int Conf 2025 Devices Integr Circuit, Devic* (2025) 380–4. doi:10.1109/DevIC63749.2025.11012484

41. Kumar R, Chandan BV, Nigam KK, Kumar A, Tanveer A, Kumar H. Design and simulation of high-sensitivity AlGaN/GaN based MOS-HEMT biosensor for biomolecule detection. *Int Conf Signal Process Commun ICSC* (2025) 791–6. doi:10.1109/ICSC64553.2025.10967903

42. Mohanty SS, Mishra S, Mishra GP. Impact of sensitivity due to the variation of structural parameters of dual material gate stack source cavity hetero MOSFET biosensor. *Sens Imaging* (2025) 26(1):1–14. doi:10.1007/s11220-025-00551-3